Predicting the response of turbulent channel flow to varying-phase opposition control: Resolvent analysis as a tool for flow control design

Simon S. Toedtli,[1,*] Mitul Luhar,[2] and Beverley J. McKeon[1]

[1]*Graduate Aerospace Laboratories, California Institute of Technology, Pasadena, California 91125, USA*

[2]*Department of Aerospace and Mechanical Engineering, University of Southern California, Los Angeles, California 90089, USA*

(Received 3 November 2018; published 31 July 2019)

The present study evaluates the capabilities of a low-order flow model based on the resolvent analysis of McKeon and Sharma [B. J. McKeon and A. S. Sharma, J. Fluid Mech. **658**, 336 (2010)] for the purpose of controller design for drag reduction in wall-bounded turbulent flows. To this end, we first show that the model is able to approximate the change in mean wall shear stress, which is commonly used as measure for drag reduction. We also derive an analytical expression that decomposes the drag reduction in internal flows into terms that can be predicted directly by the model and terms that allow for quantification of model error if high-fidelity data are available. We then show by example of varying-phase opposition control in a low-Reynolds-number turbulent channel flow that the drag reduction predicted by the resolvent model captures the trend observed in direct numerical simulation (DNS) over a wide range of controller parameters. The DNS results confirm the resolvent model prediction that the attainable drag reduction strongly depends on the relative phase between sensor measurement and actuator response, which raises interesting flow physics questions for future studies. The good agreement between the resolvent model and DNS further reveals that resolvent analysis, which at its heart is a linear technique, is able to approximate the response of the full nonlinear system to control. We also show that in order to make accurate predictions the model only needs to resolve a small subset of the DNS wave numbers and that the controlled resolvent modes obey the Reynolds-number scaling laws of the uncontrolled resolvent operator derived by Moarref *et al.* [R. Moarref *et al.*, J. Fluid Mech. **734**, 275 (2013)]. As a consequence, our results suggest that resolvent analysis can provide a suitable flow model to design feedback flow control schemes for the purpose of drag reduction in incompressible wall-bounded turbulent flows even at technologically relevant Reynolds numbers.

DOI: 10.1103/PhysRevFluids.4.073905

I. INTRODUCTION

Turbulence may be aesthetically pleasing to the observer's eye, yet it is undesired in most engineering applications. For example, turbulent drag accounts for more than 50% of the total drag force exerted on a large oil tanker [1] and thus a reduction of the turbulence level by just a few percent could lead to tremendous energetic and monetary savings. The potential benefits associated with targeted manipulations of turbulent flows have spurred enormous interest in the field of flow control for well over a century and while important advances have been made in various aspects, equally many questions remain open even at the very fundamental level (see, for example, Ref. [2]).

*stoedtli@caltech.edu

One important open question of the field is the formulation of tractable and effective flow models to enable systematic controller design for various control objectives. The present study aims at contributing towards this question and assesses the potential of a flow model based on the resolvent analysis of McKeon and Sharma [3] for the purpose of controller design. We limit the scope of this study to the class of incompressible wall-bounded turbulent flows, to the control objective of drag reduction, and to the mechanism of active feedback flow control. The resolvent model may also be useful to design controllers for other types of flows, objectives, and control mechanisms, but the assessment of such applications is beyond the scope of this study.

A. Resolvent analysis

Research efforts over the past 25 years have shown that linear mechanisms play a key role in the transition to turbulence (among others, Ref. [4]) and in the dynamics of fully developed wall-bounded turbulent flows (for example, Ref. [5]). One line of work devoted to these linear mechanisms in wall-bounded turbulence considers the amplification characteristics of the forced linear Navier-Stokes operator. Different analysis techniques and types of forcing have been proposed in the past (see Ref. [6] for an overview) and the resemblance of the associated linear responses to different features of turbulent flows has underscored the importance of linear mechanisms and the robustness of the Navier-Stokes system to the type of forcing. The foundation for this study is one particular analysis of the forced linear Navier-Stokes system, namely, the resolvent analysis of McKeon and Sharma [3]. Under the resolvent formulation, the full nonlinear Navier-Stokes equations (NSE) are rewritten as a linear operator that maps the nonlinear advection term to velocity and pressure fluctuations. Unique to this approach is that the nonlinear term is viewed as intrinsic forcing to the remaining linear system and that an efficient representation of the linear operator is obtained from identifying the directions which are most amplified by the operator in an energy norm sense. The resulting decomposition of the operator lends itself to low-order modeling and will be at the heart of the flow model considered here. A clear understanding of the method and results of this study requires basic familiarity with resolvent analysis and we therefore briefly review its key elements below by example of a fully developed turbulent channel flow with periodic boundary conditions in the wall-parallel directions.

Following McKeon and Sharma [3], we first Reynolds decompose all flow quantities into a spatiotemporal mean $\overline{(\cdot)}$ and turbulent fluctuations $(\cdot)'$. For example, $\mathbf{u}(x, y, z, t) = \overline{\mathbf{u}}(y) + \mathbf{u}'(x, y, z, t)$, where x, y, and z denote the streamwise, wall-normal, and spanwise coordinates, respectively, with corresponding components u, v, and w of the velocity vector $\mathbf{u}$, and t represents time. The streamwise mean velocity profile $\overline{u}(y)$ is assumed to be known (from an experiment, numerical simulation, or eddy viscosity model), which allows us to restrict the problem to the turbulent fluctuations.

The model development progresses by seeking an optimal basis in all three spatial dimensions and time, where the notion of optimality is defined in an energy norm sense: In each dimension, we seek that basis whose first N basis functions capture more kinetic energy $|\mathbf{u}|^2$ (under an $\mathcal{L}^2$-norm) of the flow than the first N functions of any other basis. It can be shown analytically that the Fourier basis is the optimal one in the statistically homogeneous streamwise and spanwise directions and in the stationary temporal coordinate [7]. This motivates expanding the fluctuating velocity and pressure (p') fields in terms of Fourier modes

$$\begin{bmatrix}\mathbf{u}'(x, y, z, t)\\ p'(x, y, z, t)\end{bmatrix} = \sum_{l=-\infty}^{\infty}\sum_{m=-\infty}^{\infty}\int_{-\infty}^{\infty}\begin{bmatrix}\hat{\mathbf{u}}(l, m, \omega, y)\\ \hat{p}(l, m, \omega, y)\end{bmatrix} e^{i[(2\pi/L_x)lx+(2\pi/L_z)mz-\omega t]}d\omega, \tag{1}$$

with coefficients $[\hat{\mathbf{u}}, \hat{p}]^T$. Recall that the domain is periodic in x and z, with period L_x and L_z, respectively. The periodicity restricts the streamwise (k_x) and spanwise (k_z) wave numbers to integer multiples of the fundamental wave numbers $k_x = l\,(2\pi/L_x)$ and $k_z = m\,(2\pi/L_z)$, with $\{l, m\} \in \mathbb{Z}$, and reduces the Fourier transforms in these directions to Fourier series. The temporal

coordinate is unbounded and therefore $\omega \in \mathbb{R}$. A single Fourier mode can be characterized either by its streamwise and spanwise indices and temporal frequency $[l, m, \omega]^T$ or by its wave-number vector $\mathbf{k} = [k_x, k_z, \omega]^T$, and both notations will be used interchangeably when working in Fourier domain.

The fluctuating part of the NSE can be written for each mode with $\mathbf{k} \neq \mathbf{0}$ as

$$\begin{bmatrix} \hat{u}(\mathbf{k}, y) \\ \hat{v}(\mathbf{k}, y) \\ \hat{w}(\mathbf{k}, y) \\ \hat{p}(\mathbf{k}, y) \end{bmatrix} = \underbrace{\begin{bmatrix} -i\omega + ik_x\overline{u} - \frac{\Delta}{\mathrm{Re}_\tau} & \frac{d\overline{u}}{dy} & 0 & ik_x \\ 0 & -i\omega + ik_x\overline{u} - \frac{\Delta}{\mathrm{Re}_\tau} & 0 & \frac{d}{dy} \\ 0 & 0 & -i\omega + ik_x\overline{u} - \frac{\Delta}{\mathrm{Re}_\tau} & ik_z \\ ik_x & \frac{d}{dy} & ik_z & 0 \end{bmatrix}^{-1}}_{\mathcal{H}(\mathbf{k})} \times \underbrace{\begin{bmatrix} \hat{f}_u(\mathbf{k}, y) \\ \hat{f}_v(\mathbf{k}, y) \\ \hat{f}_w(\mathbf{k}, y) \\ 0 \end{bmatrix}}_{\hat{\boldsymbol{f}}(\mathbf{k}, y)}, \tag{2}$$

where $\Delta = d^2/dy^2 - k_x^2 - k_z^2$ is the Laplacian, $\{\hat{f}_u, \hat{f}_v, \hat{f}_w\}$ denote the Fourier transforms of the nonlinear advection terms, and $\mathrm{Re}_\tau = u_\tau h/\nu$ is the Reynolds number based on the channel half-height h, friction velocity $u_\tau = \sqrt{\tau_w/\rho}$, and kinematic viscosity of the fluid ν (τ_w is the mean wall shear stress and ρ is the fluid density). As implied by Re_τ, all quantities are made dimensionless with h and u_τ and, unless stated otherwise, the same nondimensionalization will be employed in the remainder of this study. The linear operator $\mathcal{H}(\mathbf{k})$ that maps the nonlinear forcing terms to the velocity and pressure fluctuations at each $\mathbf{k}$ is called the resolvent operator. Recall that we assumed the mean velocity profile to be known and therefore $\mathcal{H}(\mathbf{k})$ is fully determined.

The optimal basis in the remaining wall-normal direction is obtained from a singular-value (Schmidt) decomposition of the resolvent operator, as suggested by McKeon and Sharma [3], and interested readers are referred to Refs. [8,9] for an in-depth discussion of the technicalities. The singular-value decomposition returns an ordered basis pair $\{\hat{\boldsymbol{\psi}}_j, \hat{\boldsymbol{\phi}}_j\}$ which can be used to rewrite Eq. (2) as

$$\begin{bmatrix} \hat{\mathbf{u}}(\mathbf{k}, y) \\ \hat{p}(\mathbf{k}, y) \end{bmatrix} = \mathcal{H}(\mathbf{k})\,\hat{\mathbf{f}}(\mathbf{k}, y) = \sum_{j=1}^{\infty} \sigma_j(\mathbf{k})\,\hat{\boldsymbol{\psi}}_j(\mathbf{k}, y)\langle\hat{\boldsymbol{\phi}}_j(\mathbf{k}, y), \hat{\mathbf{f}}(\mathbf{k}, y)\rangle, \tag{3}$$

where $\sigma_1 \geqslant \sigma_2 \geqslant \cdots > 0$ denote the singular values (gains) of $\mathcal{H}(\mathbf{k})$, $\hat{\boldsymbol{\psi}}_j = [\hat{u}_j, \hat{v}_j, \hat{w}_j, \hat{p}_j]^T$ and $\hat{\boldsymbol{\phi}}_j = [\hat{f}_{uj}, \hat{f}_{vj}, \hat{f}_{wj}, 0]^T$ are, respectively, the left and right singular vectors (wall-normal basis functions) associated with σ_j, and $\langle\cdot,\cdot\rangle$ denotes the $\mathcal{L}^2$-inner product in the wall-normal direction for vector-valued functions. We will refer to the left singular vectors $\hat{\boldsymbol{\psi}}_j$ as resolvent modes hereafter. The basis elements are ranked in order of descending gain σ_j and the singular values come in pairs of equal or at least same order of magnitude values, which is a peculiarity of the channel geometry (see Ref. [8] for details). The paired singular vectors are not unique (any linear combination of them is also a legitimate singular vector) and an additional constraint is required to ensure uniqueness. Following [8], we therefore impose an additional wall-normal symmetry constraint on the paired singular vectors, which results in distinct wall-normal symmetries of the resolvent modes: $\hat{u}_j$, $\hat{w}_j$, and $\hat{p}_j$ of the first paired mode are even while $\hat{v}_j$ is odd in y and the symmetries of all components are inverted for the second mode of the pair.

Previous work has shown that the resolvent operator at each $\mathbf{k}$ is low rank [3,8] and owing to the particular choice of bases the low-rank nature is reflected in expansion (3): Typically, the first two singular values are an order of magnitude larger than the remaining ones and it can therefore be

assumed that the flow is reasonably approximated by just the first two terms of the expansion. Since almost all singular values are paired and the corresponding singular vectors only differ in their wall-normal symmetry, it is often possible to simplify further and just consider the first singular value and vector, which gives a so-called rank-1 approximation of the operator. It will be shown in Sec. II B that a rank-1 approximation is sufficient for the purpose of this study.

While the singular values and vectors can be calculated directly from the resolvent, the nonlinear forcing $\hat{\mathbf{f}}$ is not known *a priori* and has to be modeled to make further progress. It is well known that the resolvent operator is a very selective amplifier [3] and it is therefore reasonable to assume that the exact form of forcing is irrelevant as long as the real flow contains some forcing in the dominant directions. Note, however, that there is an increasing body of work devoted to modeling the shape of the forcing to accurately reconstruct the flow field [10–12]. In the present study we seek the simplest representation of the forcing that captures the control trends for this system and therefore we use the so-called rank-1 broadband forcing model $\langle \hat{\boldsymbol{\phi}}_1(\mathbf{k}), \hat{\mathbf{f}}(\mathbf{k}) \rangle = 1 \, \forall \, \mathbf{k}$ instead of the more complex models mentioned above. To guard against a common misconception, we would like to emphasize that the resolvent formulation of the NSE with broadband forcing is not a linearization. A linearization would set $\hat{\mathbf{f}}(\mathbf{k}) = \mathbf{0}$, while the rank-1 broadband forcing assumption employed here explicitly retains the nonlinearity and models it as $\hat{\mathbf{f}}(\mathbf{k}) = \hat{\boldsymbol{\phi}}_1(\mathbf{k})$.

The resulting rank-1 broadband forcing approximation of the NSE in resolvent form (3) is given by

$$\begin{bmatrix} \hat{\mathbf{u}}(\mathbf{k}, y) \\ \hat{p}(\mathbf{k}, y) \end{bmatrix} \approx \sigma_1(\mathbf{k}) \hat{\boldsymbol{\psi}}_1(\mathbf{k}, y). \tag{4}$$

To facilitate the following discussion, we will refer to Eq. (4) as the resolvent model hereafter. We note that this approach was developed in a series of previous publications and was shown to capture many key statistical and structural features of wall-bounded turbulent flows [3,8,13]. The subject of this study is to assess whether the resolvent model is a suitable flow model to design controllers for turbulent drag reduction in internal flows. The assessment is based on a generalized version of the well-known opposition control scheme [14], which often serves as a benchmark within the flow control community and which will be briefly reviewed hereafter. It is important to point out that there is nothing particular about the choice of controller and we expect that the results generalize to any control scheme with a linear control law.

B. Opposition control and low-order modeling

The idea at the heart of opposition control is to reduce turbulent drag in wall-bounded flows by detecting and suppressing the sweeps and ejections associated with the coherent structures of the near-wall cycle. To this end the control scheme measures the wall-normal velocity at a detection plane located at a distance y_d above the wall ($y_w = \pm 1$) and applies blowing and suction with equal amplitude but opposite sign at the wall: $v(y_w) = -v(y_d)$.

Previous direct numerical simulation (DNS) studies of turbulent channel [14] and pipe [15] flow at $\mathrm{Re}_\tau \approx 180$ show that opposition control can reduce drag by up to 25%. The control effectiveness strongly depends on the sensor location: Drag reduction (DR) is only observed for sensors located below $y_d^+ \leqslant 23$ (the plus superscript denotes normalization with respect to inner units, i.e., $y^+ = y u_\tau / \nu$) and the maximum DR occurs around $y_d^+ = 15$ [16]. The range of sensor locations leading to drag reduction can be increased by reducing the controller gain [16] and the maximum DR can be increased by either using upstream sensor information [17] or adding an integral term to the control law [18]. The effectiveness of the control scheme depends on the Reynolds number and decreases with increasing Re_τ: For example, the maximum DR drops from approximately 25% at $\mathrm{Re}_\tau = 180$ to 18% at $\mathrm{Re}_\tau = 1000$ [19]. The computational cost of DNS currently inhibits studies at higher Re_τ, so DNS cannot be used to analyze and design a version of the control law for technologically relevant Reynolds numbers.

The prohibitive cost of DNS necessitates the development of low-order flow models for controller design. Grounded in the insight that linear mechanisms play a key role in wall-bounded turbulence, one line of work approaches flow control for internal flows from a linear system point of view. Lim and Kim [20] used a singular-value analysis to assess the effect of opposition control on optimal initial disturbances to the linearized NSE. In agreement with previous DNS results, their analysis shows that the growth of the disturbances, which is interpreted as a proxy for turbulence intensity, decreases for a narrow range of sensor locations y_d^+ and increases if the sensor is located too far away from the wall. In a similar manner but considering a different control strategy, Duque-Daza *et al.* [21] used the linearized NSE to study how streamwise-traveling waves of spanwise wall velocity affect the energy amplification of initial perturbations that resemble elongated streamwise vortices. Their results indicate a strong correlation between the change in energy amplification of the initial perturbation and the drag reduction observed in DNS for traveling waves of various frequencies and wavelengths. Of particular relevance for the present study is previous work by Luhar *et al.* [13], who used the resolvent model (4) to analyze opposition control in a turbulent pipe flow. In contrast to the aforementioned work, the resolvent model does not capture how control affects the growth of specific initial disturbances, but rather how control alters the response of the flow to intrinsic forcing from the nonlinear advection terms. Luhar *et al.* [13] showed that the resolvent model can qualitatively reproduce the changes in DR with sensor location and Reynolds number previously observed in DNS. They further used the resolvent model to analyze a generalized version of the opposition control law given by $\hat{v}(\mathbf{k}, y_w) = -\hat{A}_d \hat{v}(\mathbf{k}, y_d)$, where $\hat{A}_d \in \mathbb{C}$ is the complex controller gain at each Fourier mode characterized by $\mathbf{k}$ and the original opposition control scheme corresponds to $|\hat{A}_d| = 1$ and $\angle \hat{A}_d = 0$. The resolvent model predicts that the effectiveness of opposition control in turbulent pipe flow strongly depends on the phase $\angle \hat{A}_d$ between the sensor measurement and the actuation response, but this prediction has not yet been confirmed in the full nonlinear system. The same resolvent model was subsequently used by Nakashima *et al.* [22] to study the effect of suboptimal control in a turbulent channel flow and building on this work, Kawagoe *et al.* [23] used resolvent analysis to design modified versions of the suboptimal control law. In this case the agreement between resolvent prediction and DNS was mixed: The study considered two modified controllers and good agreement between the model and DNS was observed for one of them, while the two predictions deviated for the other controller. Similar ideas were recently also applied to other classes of flows. Yeh and Taira [24] used the gains of the uncontrolled resolvent operator as proxy to identify adequate control parameters for separation control over an airfoil and showed that parameter combinations with high uncontrolled gain correspond to favorable controller settings. Leclerq *et al.* [25] considered and controlled a two-dimensional incompressible open-cavity flow using structured $\mathcal{H}_\infty$ synthesis on a sequence of linear flow models, where each flow model of the sequence is based on the resolvent operator about the mean of the previous controlled flow. Their study shows that the controller is able to successfully suppress the oscillations in a sequence of five controllers.

The literature results reviewed above suggest that linear models are able to capture at least aspects of the response of internal flows to control. With regard to resolvent-based models, it remains unclear to what extent the model is able to capture the response of the nonlinear system, since the available data set for comparison (compiled in [13,22,23]) is small and shows mixed agreement. Furthermore, previous resolvent-based control designs in internal flows have been limited to low Reynolds numbers and it remains to be clarified how the approach can be generalized to technologically relevant Re_τ.

These two questions will be the main thrust of this study. Concretely, we consider the generalized opposition control law with unit gain ($|\hat{A}_d| = 1$) but nonzero phase ($\angle \hat{A}_d \neq 0$) and we will refer to this control scheme as varying-phase opposition control hereafter. The resolvent model will be used to predict the drag reduction of varying-phase opposition control in a turbulent channel flow at $\mathrm{Re}_\tau = 180$ and a DNS of the same flow and control scheme will be used to validate the predictions over a wide range of parameters, which will allow the drawing of stronger conclusions about the capabilities of the resolvent model. We also formalize an approach for wave-number

space subsampling and outline how scaling laws can be used to make resolvent model predictions at technologically relevant Reynolds numbers.

II. APPROACH

Two approaches are used to study a turbulent channel flow at $\mathrm{Re}_\tau = 180$: The resolvent model introduced in Sec. I A and a DNS. This section presents the details of the two frameworks, outlines their commonalities and differences, and describes wave-number space subsampling in the evaluation of the resolvent model.

A. Direct numerical simulation

The direct numerical simulations of the full nonlinear system are performed with a code framework developed by Flores and Jimenéz [26]. The DNS follows the method proposed by Kim *et al.* [27] and solves the NSE in a velocity-vorticity formulation by integrating the wall-normal vorticity and the Laplacian of the wall-normal velocity in time. The details about the numerical method can be found in [26]; it is only mentioned here that the streamwise and spanwise directions are discretized using a pseudospectral Fourier-Galerkin method. The DNS therefore naturally provides access to the Fourier coefficients $\hat{\mathbf{u}}(k_x, k_z, t, y)$, which greatly simplifies the connection and comparison between the DNS and the resolvent model: Leaving the order reduction in y out of the account, the two formulations differ only in the treatment of the temporal coordinate and one can map from the resolvent model to the DNS by means of an inverse Fourier transform in time.

The parameters of the DNS are chosen to match the domain size and resolution of previous numerical simulations such as [26,28]. The nondimensional size of the computational domain in the streamwise and spanwise directions is $L_x = 4\pi$ and $L_z = 2\pi$, respectively, and $N_x = N_z = 256$ Fourier modes are used in these directions. This corresponds to resolutions of $\Delta x^+ \approx 8.8$ and $\Delta z^+ \approx 4.4$ in terms of Fourier modes before dealiasing at the nominal $\mathrm{Re}_\tau = 180$ of the uncontrolled flow. A sinusoidal grid with $N_y = 172$ points is used in the wall-normal direction, which gives a resolution of $\Delta y^+_{\mathrm{min}} \approx 0.37$ at the wall and $\Delta y^+_{\mathrm{max}} \approx 3.09$ at the channel center. Note that Re_τ, as well as therefore the resolution in inner units, changes when control is applied. The resolution increases if the drag is decreased and vice versa and runs with $\mathrm{Re}_\tau > 245$ may be considered slightly underresolved. Two runs (one for $y_d^+ = 15$ and $\angle \hat{A}_d = -\pi/4$ and another for $y_d^+ = 15$ and $\angle \hat{A}_d = \pi/2$) with higher resolution ($N_x = 512$, $N_y = 272$, and $N_z = 512$) were performed to rule out the possibility of grid effects in the results and it was indeed confirmed that the results were almost identical.

The flow is driven by a constant mass flux so that the effect of control can be captured in the change of wall shear stress. All control experiments are started from the same initial condition and statistics are collected over at least ten eddy turnover times (h/u_τ) once a statistically steady state is reached. It is also worth mentioning for later comparison that the cost of a single DNS was around 120 core hours at the time of writing. The adequacy of the current settings is confirmed by comparing the results of the present DNS to the literature data of an uncontrolled channel flow at $\mathrm{Re}_\tau = 180$ by Lee and Moser [28]: The mean Reynolds stress profiles of the two DNSs are shown in Fig. 1(a) (dash-dotted blue and solid black lines). It is apparent that the two profiles are in excellent agreement throughout the channel and so are all the other statistical quantities available for comparison (data not shown).

B. Rank-1 resolvent model

The low-order flow model put to test by DNS is the rank-1 resolvent model (4) introduced in Sec. I A. Following a large body of work (e.g., [8,29,30]), we use the semiempirical turbulent eddy viscosity model proposed by Reynolds and Tiedermann [29] with parameters $\alpha = 25.4$ (constant in the van Driest wall law) and $\kappa = 0.426$ (constant in the von Kármán logarithmic law) to represent the mean velocity profile $\overline{u}$ of the resolvent operator. Such an approach may be extended to

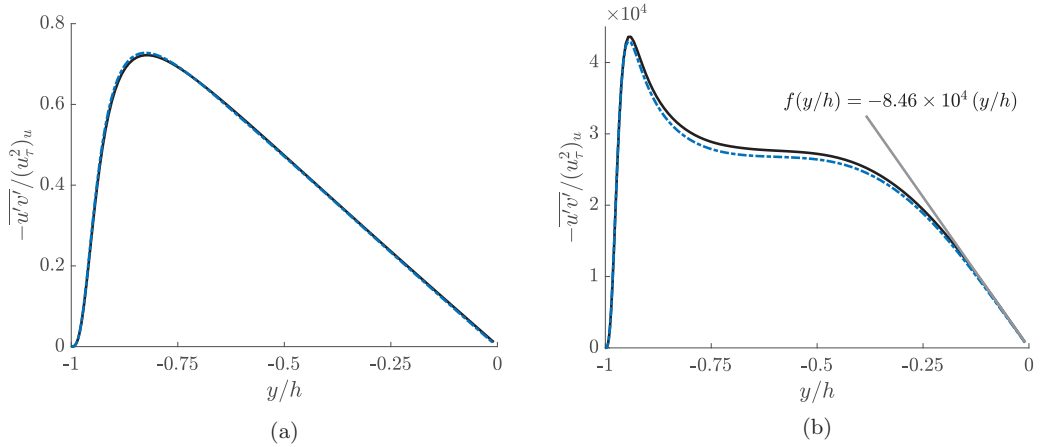

FIG. 1. Uncontrolled Reynolds stress profiles from DNS and the resolvent model: (a) - - -, DNS data of Lee and Moser [28] (uncontrolled flow); ——, present DNS (uncontrolled flow) and (b) - - -, resolvent model baseline (uncontrolled flow); ——, subsampled model (uncontrolled flow); ——, linear fit to model Reynolds stress profile in the outer flow.

regimes in which experimental or numerical results are not available and is appealing because of the analytical formulation it provides, which is readily incorporated into resolvent codes. In this study, we use the mean profile obtained using the eddy viscosity for resolvent analyses of both uncontrolled and controlled flows, i.e., we do not obtain the mean profile for the controlled flows. The latter constitutes a further modeling simplification, some implications of which are discussed below. An energy norm is chosen for the singular-value decomposition of the resolvent and the approach described by Luhar *et al.* [9] is used to compute the singular values and vectors.

As indicated earlier, a rank-1 approximation of the operator is sufficient for the present study: It will be shown in Sec. III B that in order to evaluate the effect of control on the DR, we need to compute the mean Reynolds stress profile and evaluate an integral of the form

$$I = \int_{-1}^{1} y(\overline{u'v'})dy. \tag{5}$$

For a rank-2 model the contribution of a single Fourier mode to the mean Reynolds stress $\overline{u'v'} = \widehat{uv}(\mathbf{k} = \mathbf{0})$ is proportional to

$$\begin{aligned}\widehat{uv}(\mathbf{0}, y) \sim \Re\big\{&\sigma_1^2 \hat{u}_1(\mathbf{k}, y)\hat{v}_1^*(\mathbf{k}, y) + \sigma_1\sigma_2 \hat{u}_1(\mathbf{k}, y)\hat{v}_2^*(\mathbf{k}, y) + \sigma_1\sigma_2 \hat{u}_2(\mathbf{k}, y)\hat{v}_1^*(\mathbf{k}, y) \\ &+ \sigma_2^2 \hat{u}_2(\mathbf{k}, y)\hat{v}_2^*(\mathbf{k}, y)\big\},\end{aligned} \tag{6}$$

where $\Re$ denotes the real part of a complex number and the asterisk superscript denotes its complex conjugate. Recall from the discussion about the wall-normal symmetry of resolvent modes (Sec. I A) that if the singular values are paired, then $\hat{u}_1$ and $\hat{v}_2$ are even, while $\hat{u}_2$ and $\hat{v}_1$ are odd in y. Consequently, the cross terms ($\sigma_1\sigma_2\hat{u}_1\hat{v}_2^*$ and $\sigma_1\sigma_2\hat{u}_2\hat{v}_1^*$) are even in y. The cross terms integrate to zero when weighted with y and therefore they do not contribute to the integral I. Moreover, the real parts of the two diagonal terms ($\sigma_1^2\hat{u}_1\hat{v}_1^*$ and $\sigma_2^2\hat{u}_2\hat{v}_2^*$) are equal and odd in y. The diagonal terms therefore do contribute to I, but since their real parts are equal there is no difference between a rank-1 and a rank-2 approximation. Recall that almost all singular values are paired, so the above statement is true for almost all resolvent modes; it can therefore be expected that the DR (which is based on integrals of the form I) predicted by a rank-1 and a rank-2 model is almost identical and this has indeed been confirmed in numerical experiments (data not shown). For the purpose of the present study it thus suffices to consider a rank-1 approximation, as anticipated in Sec. I A.

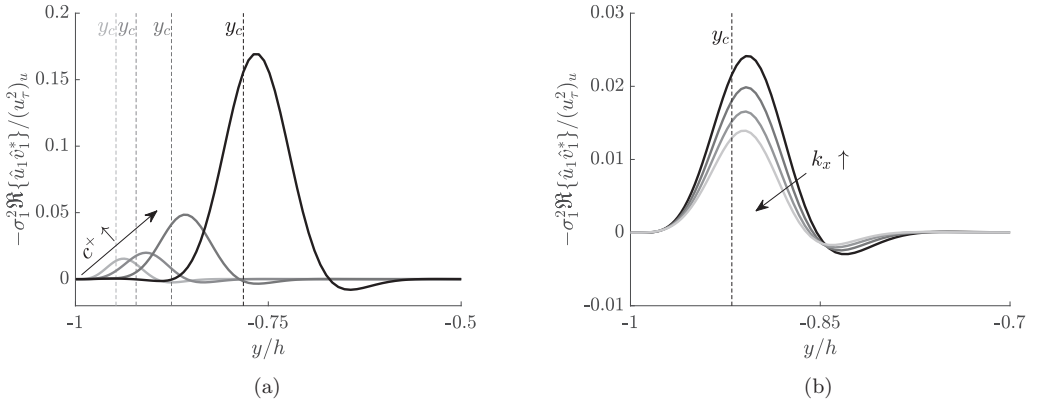

FIG. 2. Effect of wave speed and streamwise wave number on the mean Reynolds stress contribution of individual resolvent modes: (a) effect of wave speed c (for $k_x = 5.5$, $k_z = 2$, and $c^+ = \{8, 10, 12, 14\}$), with darker colors indicating faster wave speeds, and (b) effect of streamwise wave number k_x (for $k_x = \{5, 5.5, 6, 6.5\}$, $k_z = 2$, and $c^+ = 10$), with darker colors indicating smaller streamwise wave numbers.

The resolvent model uses the same numerical parameters as the DNS wherever possible, so model errors due to resolution discrepancies can be ruled out and a meaningful comparison can be made. This choice has the additional benefit that minimal empirical knowledge is required to select an appropriate set of model parameters. In this spirit, we resolve the same streamwise and spanwise wave numbers in the model as in the DNS (after dealiasing): $k_x = l/2$, $l \in [-84, 84]$, and $k_z = m$, $m \in [-84, 84]$. In practice, only the non-negative wave numbers are evaluated, since the wave-number symmetries discussed in Sec. II D can be used to account for the contribution of the negative k_x and k_z. In the wall-normal direction the resolvent operator is discretized on a set of $N_y = 172$ Chebyshev collocation points so that the grid of the model and the DNS are identical up to a stretching factor described in [28].

The only coordinate that requires empirical input for parameter selection is the temporal frequency: The continuous range of frequencies resolved in the DNS is too large to be handled reasonably by the numerical framework of the model and furthermore the DNS does not provide a well-defined sampling rate because the time step changes subject to a Courant-Friedrichs-Lewy (CFL) condition. However, there is compelling empirical evidence that the temporal frequency content of each Fourier mode is approximately sparse, so the entire frequency spectrum does not need to be resolved. As summarized by Bourguignon *et al.* [31], the dominant temporal frequencies at $k_x \neq 0$ can be parametrized by the wave speed $c = \omega/k_x$ and fall within the empirical range $10 \leqslant c \leqslant U_{\text{cl}}$, where U_{cl} is the channel centerline velocity. This suggests picking the temporal frequency vector ω at each k_x such that at least the range $10 \leqslant \omega/k_x \leqslant U_{\text{cl}}$ can be resolved. For reasons that will become clear shortly, we use the slightly more conservative range $0 \leqslant \omega/k_x \leqslant U_{\text{cl}}$ in this study. Note that since the range of wave speeds is kept constant across all $\mathbf{k}$, the corresponding temporal frequencies change for different k_x.

An appropriate sampling rate in c can be derived from the wall-normal localization of the resolvent modes: Fig. 2(a) shows that the mean Reynolds stress contribution of a single resolvent mode is localized around its critical layer, i.e., around the wall-normal location y_c, where its wave speed equals the local mean velocity $c \approx \overline{u}(y_c)$. Conversely, one can say that the dominant contribution to the Reynolds stress at a fixed y comes from modes whose critical layer y_c corresponds to that y. The discretization of the wall-normal coordinate naturally samples the mean velocity profile and defines the critical wave speeds that are resolved by the grid. From the previous argument we expect that the dominant Reynolds stress contribution at each grid point y_i is given by modes with wave speed $c = \overline{u}(y_i)$. This suggests that the sampled wave speeds should correspond to

the discretized mean velocity profile so that $0 \leqslant \omega \leqslant k_x U_{\mathrm{cl}}$ (as mentioned before) and $\Delta\omega_i(k_x) = k_x \Delta\overline{u}(y_i)$. Note that empirical knowledge is only required to justify this range of ω; no empirical knowledge is required to evaluate it. The temporal frequency vector is fully determined by the given mean velocity profile and wall-normal grid.

The exceptions to the above discussion are the streamwise constant modes ($k_x = 0$). For such modes the wave speed c is not well defined and a different, for now empirical, approach is needed to determine an appropriate frequency vector. The amplification of streamwise constant modes peaks at $\omega = 0$ and drops off very quickly and symmetrically as ω moves away from the origin. For example, the maximum σ_1 across all k_z drops from $\sigma_1 = 696$ at $\omega = 0$ to $\sigma_1 = 34$ at $\omega = \pm 0.4$ and $\sigma_1 = 2$ at $\omega = \pm 3.5$ and further decreases as $|\omega|$ increases (data not shown in the interest of brevity). Recall that the Reynolds stress contribution depends on the square of the singular value and therefore contributions beyond $\omega = \pm 3.5$ can be neglected. We thus restrict the temporal frequency vector of $k_x = 0$ to $-3.5 \leqslant \omega \leqslant 3.5$ and sample densely around the origin ($\Delta\omega = 0.01$ for $-0.25 \leqslant \omega \leqslant 0.25$) and more coarsely away from it ($\Delta\omega = 0.05$ for $0.3 \leqslant |\omega| \leqslant 0.5$ and $\Delta\omega = 0.25$ for $0.75 \leqslant |\omega| \leqslant 3.5$).

It was verified that the results presented in this study do not depend on the particular choice of ω: Across all k_x the DR obtained for various $\angle\hat{A}_d$ varies only minimally if the bandwidth of ω is increased or if the sampling frequency $\Delta\omega$ is changed. For reasons that will become more clear in Sec. II C, we will refer to resolvent model runs with the above parameter settings as the model baseline. Also, for future reference it is worth mentioning that one model baseline run costs around 160 core hours at the time of writing, i.e., the evaluation of the model baseline and DNS is similarly expensive at this Re_τ.

The Reynolds stress profile predicted by the model baseline for an uncontrolled channel flow at $\mathrm{Re}_\tau = 180$ is shown as a dash-dotted blue line in Fig. 1(b). The model baseline resolves all dynamically relevant spatial and temporal scales and therefore can be considered a resolvent model prediction at DNS resolution. However, it is apparent from the figure that the model profile does not match the DNS Reynolds stress: The model overpredicts the peak magnitude [compare the y axes of Figs. 1(a) and 1(b)] and the modeled profile peaks closer to the wall than the real one and exhibits a plateau within $-0.75 \leqslant y/h < -0.4$ instead of a near-linear decrease. Recall that the model is not constrained to satisfy the mean momentum equation, since we neglected the latter in the model development. However, it is interesting to note that the modeled Reynolds stress still exhibits a near-linear decrease in the outer flow, as indicated by the gray line in Fig. 1(b). In agreement with the overpredicted magnitude of the Reynolds stress, the slope is steeper than what one would expect from an analysis of the mean momentum equation. These observations are in agreement with previous results from a similar study of a turbulent pipe flow by Luhar *et al.* [13]. The only difference from the pipe flow result is the heavier tail in the outer channel ($y/h > -0.5$), which can be ascribed to the streamwise constant ($k_x = 0$) modes with zero temporal frequency and low spanwise wave numbers: These dominant streamwise constant modes peak close to the channel center and have the largest singular values of all resolved wave numbers. Under the broadband forcing assumption their contributions have a strong footprint on the integrated Reynolds stress profile and therefore give rise to the observed heavy tail. The role of the $k_x = 0$ modes within the resolvent framework remains to be fully understood and an in-depth analysis is beyond the scope of this investigation, but we would like to point out that the largest amplification occurring for streamwise constant modes is reminiscent of transient growth, where streamwise constant vortices are well known to be the optimal perturbations [32].

Given that the resolvent model is not constrained to satisfy the mean momentum equation and the numerous model assumptions, in particular the broadband forcing, the observed deviations between the model and DNS profile may not be surprising. Nevertheless, in view of recent work on more complex forcing models that approximate the correct flow statistics [10–12] one may ask whether a rank-1 model with broadband forcing is still adequate. However, the key point not to forget in a control context is this: A useful control-oriented model mainly needs to capture the relation between inputs and outputs; it need not produce the correct flow statistics of the system [33]. In this spirit the

goal should be to find the simplest possible model that is able to approximate the response of the full nonlinear system to control and in this sense the broadband forcing assumption is preferred over the aforementioned more complex models. Furthermore, unlike the other models, the broadband forcing assumption does not require flow data as input, which minimizes the dependence on empirical data.

C. Subsampling in wave-number space

While the model baseline is the appropriate starting point for comparison with DNS, its evaluation is computationally too expensive for practical purposes like parameter studies or controller design at higher Re_τ. An analysis of the mean Reynolds stress contribution of individual resolvent modes reveals that their contribution varies smoothly in at least parts of the wave-number space. This observation suggests that the resolvent model could take advantage of subsampling across wave-number space to reduce the number of resolved scales compared to the DNS. This approach has already been used in previous studies (for example, [8,13]), but without formal justification. The goal of this section is to demonstrate that subsampling is indeed appropriate.

As can be seen from Fig. 2(a), the mean Reynolds stress contribution of a single mode is localized around the critical layer y_c and therefore its wall-normal profile is mainly determined by the wave speed c. The wall-normal profiles for different c look very similar and the location of their peak moves slowly away from the wall as the wave speed is increased. This suggests that not all the wave speeds resolved in the model baseline are required to capture the wall-normal shape of the mean Reynolds stress profile, since resolvent modes with similar wave speeds largely overlap in y. Figure 2(b) further shows the mean Reynolds stress contribution for modes with various k_x at fixed k_z and c. It is again apparent that the wall-normal localization of the modes is fixed by the wave speed. Furthermore, it can be seen that the wall-normal profiles look very similar for various k_x and that the peak magnitude slowly decreases as k_x increases. This observation holds for all sufficiently large streamwise and spanwise wave numbers ($k_x \gtrapprox 5$ and $k_z \gtrapprox 10$) and suggests that the spatial wave numbers can be subsampled as well as the wave speeds.

Based on these insights, the wave-number space is subsampled as follows to evaluate the mean Reynolds stress (the contributions of negative frequencies can be obtained from the symmetries discussed next): $k_x = [0, 0.5, \ldots, 5, 7.5, 10, 20, 31, 42]$, $k_z = [0, 1, \ldots, 10, 12, 14, 16, 20, 25, 30, 40, 50, 60, 70, 84]$, and only every other value of $\overline{u}(y)$ is used to populate c. This corresponds to a reduction from $85 \times 85 \times 86$ (baseline) to $16 \times 22 \times 44$ (subsampled model) resolved wave numbers. The missing wave numbers are linearly interpolated and ω is not subsampled if $k_x = 0$.

The resulting Reynolds stress profile of the uncontrolled flow is shown as a solid black line in Fig. 1(b). The good agreement with the model baseline (dash-dotted blue line) confirms that the wave-number space can indeed be sampled very sparsely. The subsampled model only resolves about 2% of the wave numbers of the baseline, which reduces the computational time to 2 core hours. This is cheap enough to allow, for example, extensive parameter searches for controller design. Furthermore, the memory requirements and operation count of the subsampled model are small enough so that it can be run on an off-the-shelf laptop and no high-performance computing facilities are required to evaluate it.

Motivated by the results of this section, we will use the subsampled model for all resolvent predictions hereafter and we will make all comparisons between the subsampled resolvent model and DNS.

D. Wave-number symmetries

Before moving on to the description of the control scheme, we take a closer look at the wave-number symmetries of the DNS and the resolvent model. The different symmetries present in the two frameworks will have a bearing on the formulation of the control scheme and, generally speaking, are an important constraint to keep in mind when linking the resolvent model and DNS.

The first wave-number symmetry, which is present in both the DNS and the resolvent model, follows from the properties of the Fourier transform: The Fourier coefficients of the velocity and pressure fluctuations are Hermitian symmetric, because the underlying physical quantities are real-valued functions. For example, the Fourier coefficients of the velocity field satisfy $\hat{\mathbf{u}}(-k_x, -k_z, t, y) = \hat{\mathbf{u}}^*(k_x, k_z, t, y)$ (DNS) and $\hat{\mathbf{u}}(-\mathbf{k}, y) = \hat{\mathbf{u}}^*(\mathbf{k}, y)$ (resolvent model). A second symmetry, which is present in the resolvent model but not in the DNS, follows from the structure of the resolvent operator $\mathcal{H}(\mathbf{k})$ and the broadband forcing assumption: Evaluating Eq. (2) at $\tilde{\mathbf{k}} = [k_x, -k_z, \omega]^T$ instead of $\mathbf{k} = [k_x, k_z, \omega]^T$ only changes the sign of two off-diagonal terms in the resolvent operator. The sign change can be absorbed into the coefficient vectors by making the substitutions $\hat{\mathbf{u}}^\dagger(\tilde{\mathbf{k}}, y) = [\hat{u}, \hat{v}, -\hat{w}, \hat{p}]^T$ and $\hat{\mathbf{f}}^\dagger(\tilde{\mathbf{k}}, y) = [\hat{f_u}, \hat{f_v}, -\hat{f_w}, 0]$ so that $\hat{\mathbf{u}}^\dagger(\tilde{\mathbf{k}}, y) = \mathcal{H}(\mathbf{k})\hat{\mathbf{f}}^\dagger(\tilde{\mathbf{k}}, y)$. The broadband forcing assumption sets $\hat{\mathbf{f}}^\dagger(\tilde{\mathbf{k}}, y) = \hat{\mathbf{f}}(\mathbf{k}, y)$ and thus imposes the additional symmetry $\hat{\mathbf{u}}^\dagger(\tilde{\mathbf{k}}, y) = \hat{\mathbf{u}}(\mathbf{k}, y)$.

As a consequence of these two symmetries, the phase of a resolvent mode has a clear interpretation in physical domain. To see this, we consider the example of the wall-normal velocity component and write the rank-1 approximation as $\hat{v}_1(\mathbf{k}, y) = \hat{v}_1(\tilde{\mathbf{k}}, y) = A_1 e^{i\phi_1}$, where $\{A_1, \phi_1\} \in \mathbb{R}$. Evaluating the inverse Fourier transform (1) of only $\hat{v}_1(\mathbf{k}, y)$, $\hat{v}_1(\tilde{\mathbf{k}}, y)$, and their complex conjugates gives a structure $v_{\mathbf{k}}^{\mathrm{RES}}$ in the physical domain

$$v_{\mathbf{k}}^{\mathrm{RES}}(x, y, z, t) = 4A_1 \cos(k_x x - \omega t + \phi_1) \cos(k_z z), \tag{7}$$

where the factor 4 results from Hermitian symmetry and the trigonometric sum-to-product identity. Due to the symmetries, the phase ϕ_1 only enters the first term and a nonzero ϕ_1 can be interpreted as a streamwise or temporal shift of the structure. Conversely, it is apparent that the spanwise position of the structure is unaffected by a change in ϕ_1.

With regard to the DNS, the situation is more complex: Even though the DNS Fourier coefficients are symmetric in k_z in a statistical sense, their instantaneous values are unrelated, i.e., $\hat{\mathbf{u}}(k_x, -k_z, t, y) \neq \hat{\mathbf{u}}(k_x, k_z, t, y)$, and the missing symmetry in k_z complicates the interpretation of the phase in the physical domain. To see this we consider again the wall-normal velocity component and introduce the notation $\hat{v}(k_x, k_z, t, y) = A_1 e^{i\phi_1}$ and $\hat{v}(k_x, -k_z, t, y) = A_2 e^{i\phi_2}$, where $\{A_1, A_2, \phi_1, \phi_2\} \in \mathbb{R}$. Evaluating the inverse Fourier transform (1) of only $\hat{v}(k_x, k_z, t, y)$, $\hat{v}(k_x, -k_z, t, y)$, and their complex conjugates gives again a structure $v_{[k_x,k_z]}^{\mathrm{DNS}}$ in the physical domain

$$\begin{aligned} v_{[k_x,k_z]}^{\mathrm{DNS}}(x, y, z, t) = {} & 4A_1 \cos\left(k_x x + \frac{\phi_1 + \phi_2}{2}\right) \cos\left(k_z z + \frac{\phi_1 - \phi_2}{2}\right) \\ & + 2(A_2 - A_1) \cos(k_x x - k_z z + \phi_2), \end{aligned} \tag{8}$$

where we can assume $A_1 < A_2$ without loss of generality. The first summand, in which x and z factor into different terms, is the equivalent of $v_{\mathbf{k}}^{\mathrm{RES}}$. The phases of the Fourier coefficients ϕ_1 and ϕ_2 have a clear physical interpretation for this structure: If the mean of the two phases changes, the structure is shifted in the streamwise direction, and if their difference changes, the structure is shifted in the spanwise direction. Due to the missing symmetry in k_z, an additional term with mixed arguments in x and z appears which has no counterpart in the resolvent model. For this structure there is no clear interpretation of the phase either: Since the argument is mixed, a change in ϕ_2 can correspond to a streamwise or spanwise shift.

Note that Eq. (8) is a generalization of $v_{\mathbf{k}}^{\mathrm{RES}}$ and the latter can be recovered by setting $A_2 = A_1$ and $\phi_2 = \phi_1$. Whenever the (broadband forcing) resolvent model and DNS are linked, it should therefore be kept in mind that the model only represents a subset of the real physics and caution is required to ensure that the same problem is studied in both frameworks.

III. CONTROL LAW

After characterizing the two frameworks to be compared, we formally introduce the varying-phase opposition control law and the DR measure in this section.

A. Varying-phase opposition control

As mentioned in Sec. I B, Luhar *et al.* [13] studied varying-phase opposition control in a pipe flow by means of the resolvent model. They defined the control law as $\hat{v}(\mathbf{k}, y_w) = -\hat{A}_d \hat{v}(\mathbf{k}, y_d)$, with $\hat{A}_d = e^{i\phi}$ for all $\mathbf{k}$, and one may think that the same control law can be incorporated directly in the DNS. However, the control law is a good example of the importance of the wave-number symmetries discussed in Sec. II D and due to the different symmetries present in the DNS and resolvent model, additional care is required to ensure that both frameworks incorporate the same physics.

The previous discussion about symmetries shows that a phase shift $\angle \hat{A}_d = \phi$ in the resolvent model has a clear physical interpretation: Eq. (7) implies that multiplying the Fourier coefficient with a nonzero phase corresponds to a streamwise or temporal shift of the mode. A phase shift between the actuator and sensor in the Fourier domain can therefore be thought of as a streamwise or temporal lead or lag of the actuation in physical domain. However, this physical interpretation is lost when applying the same control law in the DNS, due to the missing symmetry in k_z: In addition to the streamwise shift, the mixed-argument term in Eq. (8) introduces a spanwise shift between the sensor and the actuator, which cannot be captured by the resolvent model. In order to guarantee a streamwise-only shift in the DNS so that the same physics is studied in both frameworks, the varying-phase opposition control law has to be modified slightly,

$$
\begin{aligned}
\hat{v}(\mathbf{k}, y_w) &= -\hat{A}_d^{\mathrm{RES}} \hat{v}(\mathbf{k}, y_d), \\
\hat{A}_d^{\mathrm{RES}} &= \begin{cases} 0 & \text{if } k_x = k_z = 0 \\ 1 & \text{if } k_x = 0, \quad k_z \neq 0 \\ e^{i\phi} & \text{otherwise,} \end{cases} \\
\hat{v}(k_x, k_z, t, y_w) &= -\hat{A}_d^{\mathrm{DNS}} \hat{v}(k_x, k_z, t - \Delta t, y_d), \\
\hat{A}_d^{\mathrm{DNS}} &= \begin{cases} 0 & \text{if } k_x = k_z = 0 \\ 1 & \text{if } k_x = 0, \quad k_z \neq 0 \\ e^{i\phi} & \text{if } k_x \neq 0, \quad k_z = 0 \\ \frac{\min[|\hat{v}(k_x,k_z,t-\Delta t,y_d)|, |\hat{v}(k_x,-k_z,t-\Delta t,y_d)|]}{|\hat{v}(k_x,k_z,t-\Delta t,y_d)|} e^{i\phi} & \text{otherwise,} \end{cases}
\end{aligned}
\tag{9}
$$

where the formulation for the resolvent model (RES) is shown at the top and the equivalent formulation for the DNS at the bottom.

The particular values for $\hat{A}_d$ are explained as follows. In order to ensure that control does not change the net mass flux of the flow we have to set $\hat{A}_d = 0$ if $k_x = k_z = 0$. No phase shift, i.e., $\hat{A}_d = 1$, is applied to the remaining streamwise constant modes ($k_x = 0$ and $k_z \neq 0$), since a nonzero phase would by definition lead to a spanwise shift (at least in the DNS). The values of $\hat{A}_d$ for $k_x \neq 0$ are chosen such that a streamwise shift is guaranteed: A streamwise shift is ensured for the spanwise constant modes ($k_x \neq 0$ and $k_z = 0$) of the DNS and we can therefore set $\hat{A}_d^{\mathrm{DNS}} = e^{i\phi}$ for those modes. The last value of $\hat{A}_d^{\mathrm{DNS}}$ requires some more explanation. Spanwise shifts can be prevented if the control input only generates the first term of Eq. (8). This can be achieved by setting $A_2 = A_1$, i.e., enforcing $|\hat{v}(k_x, k_z, y_w, t)| = |\hat{v}(k_x, -k_z, y_w, t)|$. While either amplitude would be a valid choice, it is desirable from a control perspective to pick the smaller of the two in order to ensure a minimal controller input. The particular choice of $\hat{A}_d$ ensures just that and sets $A_2 = A_1 = \min[|\hat{v}(k_x, k_z, y_d, t)|, |\hat{v}(k_x, -k_z, y_d, t)|]$ in Eq. (8). Note that this choice leaves the mixed-argument term uncontrolled, but ensures a streamwise-only shift. The value of $\hat{A}_d$ for the $k_x \neq 0$ resolvent modes is simpler to explain: Recall from Eq. (7) that the additional symmetry of the resolvent modes ensures a streamwise shift, so we can set $\hat{A}_d^{\mathrm{RES}} = e^{i\phi}$ for all $k_x \neq 0$ modes.

Two comments are important to mention before moving on to the DR measure. First, following [13], the potential changes in the mean velocity profile and nonlinear forcing due to control are, for simplicity, not incorporated in the resolvent model. In other words, the uncontrolled mean velocity profile and broadband forcing assumption are also used in the controlled cases and the controlled

and uncontrolled resolvent models differ only in the boundary conditions on v. Second, note that there is a time delay of one time step between the sensor measurement and the actuator response in the DNS, because the actuation is implemented as a Dirichlet boundary condition. The time delay is equivalent to an additional frequency-dependent phase $e^{i\omega\Delta t}$ in the Fourier domain, which is not represented in the resolvent model. The time step Δt varies subject to a CFL condition, but is of the order 10^{-3}. The phase error introduced to the structures of the near-wall cycle, which are expected to dominate the control signal and can be characterized by $\lambda_x^+ \approx 1000$ and $c^+ \approx 10$–12 [13], is $\omega\Delta t \approx \pi/450$. This is two orders of magnitude smaller than the phase shifts induced by the controller and it can therefore be expected that the phase error due to the time delay is negligible. Simulations with smaller Δt and therefore smaller phase errors were performed to validate this assumption and it was indeed confirmed that the drag reduction obtained for smaller Δt was nearly the same.

B. Drag reduction measure

Following previous DNS studies [14,16], we quantify the DR in terms of change in mean wall shear stress. For a constant mass flux channel flow, we can use the Fukagata-Iwamoto-Kasagi (FIK) identity [34] (adjusted to the coordinate system and nondimensionalization of the present paper) to express the change in mean wall shear stress as

$$\Delta\tau = \frac{(\tau_w)_u - (\tau_w)_c}{(\tau_w)_u} = \frac{\int_{-1}^{1} y[(\overline{u'v'})_u - (\overline{u'v'})_c]dy}{\frac{\mathrm{Re}_b}{(\mathrm{Re}_\tau^2)_u} + \int_{-1}^{1} y(\overline{u'v'})_u dy}, \tag{10}$$

where we used the friction velocity of the uncontrolled flow $(u_\tau)_u$ to nondimensionalize all velocities (the subscripts u and c label quantities of the uncontrolled and controlled flows, respectively) and where $\mathrm{Re}_b = 2U_b h/\nu$ is the Reynolds number based on twice the bulk velocity U_b. As explained in [34], the denominator of Eq. (10) is a sum of a laminar contribution (first term), fully determined by the mean velocity profile, and a turbulent contribution (second term), fully determined by the weighted integral of the Reynolds stresses.

The discussion in Sec. II B underpinned that the resolvent model does not satisfy the mean momentum equation and Fig. 1 in particular demonstrated that the modeled Reynolds stress does not match the true one. As a consequence, the resolvent model does not predict the correct relative magnitude of the laminar and turbulent drag contribution and it would therefore not be meaningful to evaluate the DR according to Eq. (10). Instead, we use the mean momentum equation to recast Eq. (10) into a more appropriate form for the purpose of the present study

$$\begin{aligned}\Delta\tau = &\underbrace{\frac{\int_{-1}^{1} y[(\overline{u'v'})_u - (\overline{u'v'})_c]dy}{\int_{-1}^{1} y(\overline{u'v'})_u dy}}_{=T_1(y_d,\angle\hat{A}_d)} \underbrace{\left(1 - \frac{3}{2}\frac{\mathrm{Re}_b}{\left(\mathrm{Re}_\tau^2\right)_u}\right)}_{=T_2} \\ &\times \underbrace{\frac{\int_{-1}^{1} y[(\overline{u'v'})_u^{\mathrm{DNS}} - (\overline{u'v'})_c^{\mathrm{DNS}}]dy}{\int_{-1}^{1} y[(\overline{u'v'})_u - (\overline{u'v'})_c]dy}}_{=T_3(y_d,\angle\hat{A}_d)} \underbrace{\frac{\int_{-1}^{1} y(\overline{u'v'})_u dy}{\int_{-1}^{1} y(\overline{u'v'})_u^{\mathrm{DNS}} dy}}_{=T_4},\end{aligned} \tag{11}$$

where the superscript DNS labels a quantity that is obtained from DNS and which therefore satisfies the mean momentum equation. This is in contrast to quantities without a superscript label which, depending on the context, originate from DNS or the resolvent model. The term $T_1(y_d, \angle\hat{A}_d)$ represents the turbulent DR predicted by the model under consideration (resolvent or DNS) and as such depends on the sensor location y_d and the phase shift $\angle\hat{A}_d$. The second term T_2 is the ratio of the turbulent drag to the total drag in the real uncontrolled flow, which is a constant for fixed Re_b. The product $T_1(y_d, \angle\hat{A}_d)T_2$ represents the total change in wall shear stress, possibly subject to model errors represented by the last two terms: $T_3(y_d, \angle\hat{A}_d)$ is the model error in turbulent DR, which is a

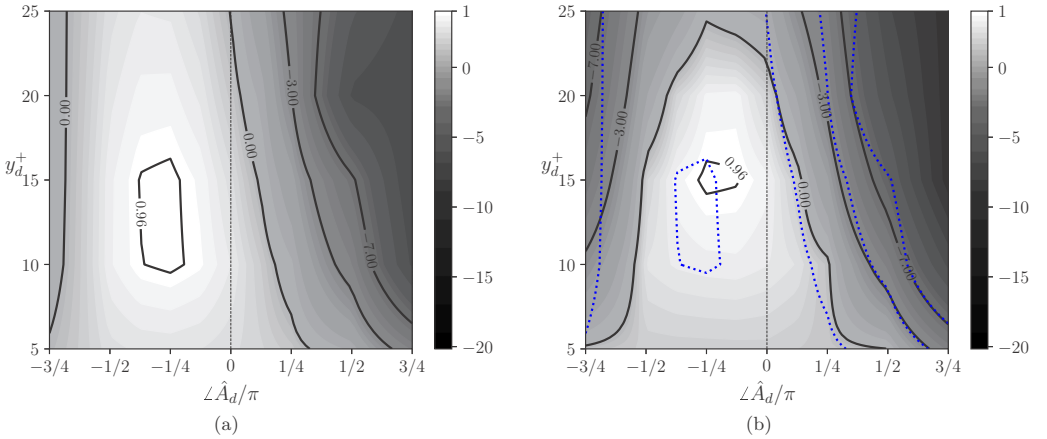

FIG. 3. Contour map showing the normalized drag reduction ξ as a function of sensor location y_d^+ and phase shift $\angle\hat{A}_d$ for (a) the prediction of the resolvent model and (b) the DNS data. Note that the color scale is nonlinear in order to highlight the region of drag reduction. The vertical dashed black line denotes $\angle\hat{A}_d = 0$, which is closely related to opposition control, and the contour lines of (a) are replotted as dotted blue lines in (b). Nondimensionalization to inner units is based on $(u_\tau)_u$ of the uncontrolled flow and the maximum DR used to normalize the contour maps is (a) resolvent model max DR = 5% and (b) DNS max DR = 21%.

function of the control parameters, and the constant T_4 is the model error in the uncontrolled profile. Note that for DNS data $T_3(y_d, \angle\hat{A}_d) = T_4 = 1$, so the usual definition for DR is recovered.

With DNS data we can evaluate all terms of Eq. (11), while with the resolvent model we can evaluate $T_1(y_d, \angle\hat{A}_d)$, which solely depends on model data, and T_2, which can be obtained from the input $(\mathrm{Re}_\tau)_u$ and the corresponding mean profile. The model errors $T_3(y_d, \angle\hat{A}_d)$ and T_4 cannot be obtained from the resolvent model alone. In other words, with the resolvent model we can estimate the change in mean wall shear stress up to a model error

$$\mathrm{DR} = T_1(y_d, \angle\hat{A}_d)T_2 = \frac{\Delta\tau}{T_3(y_d, \angle\hat{A}_d)T_4}. \tag{12}$$

From here on, the term drag reduction will be used to denote the quantity in Eq. (12). When comparing different control configurations, as will be done in Sec. IV, it is advantageous to normalize the DR by a reference value, for example the maximum DR (max DR for short) obtained over the parameter space considered

$$\xi = \frac{\mathrm{DR}}{\max \mathrm{DR}} = \frac{\Delta\tau}{\max \Delta\tau}\frac{T_3(y_{d,\max}, \angle\hat{A}_{d,\max})}{T_3(y_d, \angle\hat{A}_d)}. \tag{13}$$

This allows the elimination of T_4, the model error in the uncontrolled profile.

IV. RESULTS AND DISCUSSION

A. Comparison between the rank-1 resolvent model and DNS

The varying-phase opposition control scheme (9) introduced in the preceding section is used as a test to evaluate the capabilities of the resolvent model for controller design. To this end, a total of 50 varying-phase opposition control runs covering a parameter range of five sensor locations $y_d^+ = [5, 10, 15, 20, 25]$ and ten phase shifts $\angle\hat{A}_d = [-3\pi/4, -\pi/2, -3\pi/8, -\pi/4, -\pi/8, 0, \pi/8, \pi/4, \pi/2, 3\pi/4]$ were performed in the subsampled resolvent model and the DNS. The raw DR data were subsequently interpolated using bilinear splines and normalized with the respective maximum DR to generate the two contour maps of

ξ shown in Fig. 3. The capabilities of the resolvent model will be judged based on the overall agreement between the two maps.

It should be mentioned that the largest drag increase among all DNS runs was observed for $\angle\hat{A}_d = 3\pi/4$ and $y_d^+ = [20, 25]$. The Re_τ of these runs increased by more than a factor of 2 and the simulations developed numerical instabilities due to insufficient grid resolution before a statistically steady state was reached. The two runs were not repeated with higher resolution, first because the DR trend could already be estimated from the partially completed runs and second because the exact flow statistics of parameter combinations leading to high drag increase are not of particular interest to this study. Instead, the maximum drag increase observed in all successfully completed runs was assigned to these two control cases (which is a lower bound for the effective drag increase) and the saved computational time was used towards additional runs in the parameter region of most interest (note the higher resolution in $\angle\hat{A}_d$ within the range $-\pi/2 \leqslant \angle\hat{A}_d \leqslant \pi/4$).

The resulting map of ξ as a function of y_d and $\angle\hat{A}_d$ is shown in Fig. 3, where Fig. 3(a) is the resolvent model prediction and Fig. 3(b) shows the DNS results. Recall from Eq. (13) that each map is normalized by its maximum DR, which corresponds to 5% [resolvent model, Fig. 3(a)] and 21% [DNS, Fig. 3(b)], respectively. Bright shading (positive numbers) represent drag reduction, while dark colors (negative numbers) indicate drag increase. The solid black lines outline a few selected contour levels and the contour lines of Fig. 3(a) are replotted as dotted blue lines in Fig. 3(b) to facilitate comparison between resolvent model and DNS. Note that the contour levels of both plots are identical.

Figure 3 shows that the resolvent model is able to capture the trend observed in DNS over a wide range of parameters: In both frameworks, the effect of the controller strongly depends on the phase shift $\angle\hat{A}_d$ and generally speaking a small negative shift (e.g., $\angle\hat{A}_d = -\pi/4$) leads to improved drag reduction, while a positive phase shift deteriorates the control performance and eventually leads to drag increase. Furthermore, both frameworks show that for a fixed positive phase shift $\angle\hat{A}_d > 0$ the control performance decreases as y_d increases, while for a fixed negative phase shift $-\pi/2 \leqslant \angle\hat{A}_d < 0$ the control performance initially increases, reaches a maximum, and then decreases as the sensor moves away from the wall. The qualitative agreement between the resolvent model and DNS can be made more clear by comparing the overlaid contour lines in Fig. 3(b): It is apparent that the contours of ξ of the resolvent model and the DNS collapse for $\angle\hat{A}_d > 0$ over the entire range of y_d. This suggests that the model error in turbulent DR, $T_3(y_{d,\max}, \angle\hat{A}_{d,\max})/T_3(y_d, \angle\hat{A}_d)$, is constant and approximately equal to unity for positive phase shifts. Further note that $T_3(y_{d,\max}, \angle\hat{A}_{d,\max})$ is a constant and therefore $T_3(y_d, \angle\hat{A}_d) \approx$ const for all positive shifts. The agreement between the resolvent model and DNS is reduced for negative phase shifts: The contour levels do not overlap for $\angle\hat{A}_d < -\pi/4$ and the model error in turbulent DR increases for more negative $\angle\hat{A}_d$. However, the resolvent model is still able to capture the trend of the DNS reasonably well and also the parameter combination leading to maximum drag reduction is similar in both frameworks and corresponds to $y_d^+ \approx 10 - 15$ and $\angle\hat{A}_d \approx -\pi/4$.

The explanation of the optimal sensor location and phase shift is beyond the scope of the present work, as is a more complete understanding of the physics of the phase shifts. The multimode nature of the problem complicates signaling time (ballistic) arguments, which would attempt to explain the optimal sensor location and phase shift by relating the time the control signal requires to travel from the wall to the sensor location to the time a dominant flow structure requires to travel the streamwise shift between the sensor and actuator. Yet it cannot currently be ruled out that control mainly acts on the near-wall modes and a more detailed analysis of the optimal phase shift and sensor location is left for future work.

While the resolvent model is able to capture the qualitative trend of the DNS, it underestimates the absolute DR values observed in the real flow. For example, the resolvent model predicts a maximum DR of 5% at the aforementioned optimal parameter combination $y_d^+ = 15$ and $\angle\hat{A}_d = -\pi/4$, while a 21% DR is observed in the DNS. In combination with Fig. 3(b), which shows that the resolvent model underpredicts $|\xi|$, it follows that the model underpredicts the drag reduction over the entire parameter range. We can therefore conclude from Eq. (12) that the model error terms

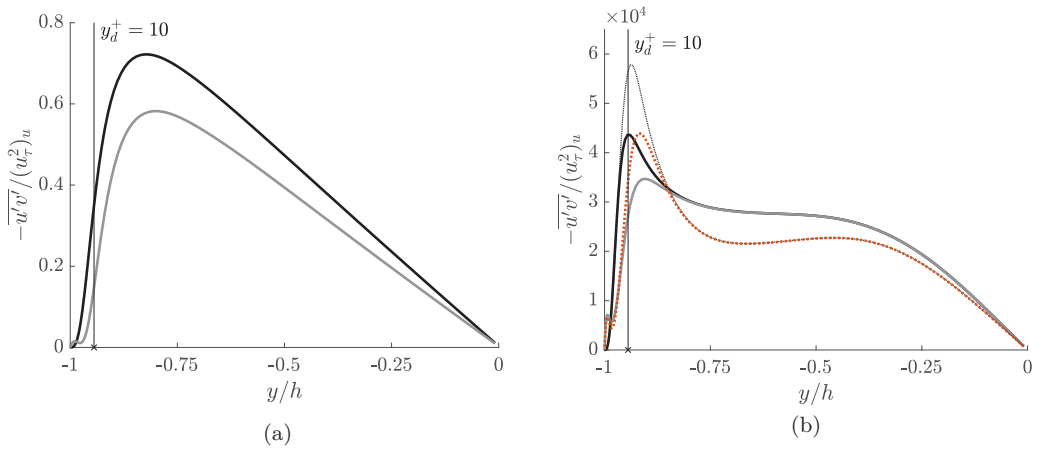

FIG. 4. Reynolds stress profiles of the uncontrolled flow and an example controlled flow ($y_d^+ = 10$ and $\angle\hat{A}_d = -\pi/4$) from DNS and the resolvent model: (a) ——, present DNS (uncontrolled flow); ——, present DNS (controlled flow) and (b) ——, subsampled model (no-slip boundary conditions (BCs) with uncontrolled mean); ——, subsampled model (control BCs with uncontrolled mean); ……, subsampled model (no-slip BCs with controlled mean); ……, subsampled model (control BCs with controlled mean). The vertical line indicates the sensor location y_d^+, where $(u_\tau)_u$ of the uncontrolled flow is used to nondimensionalize to inner units.

$T_3(y_d^+, \angle\hat{A}_d)\, T_4 > 1$ for all phase shifts considered. These error terms have a geometric interpretation in the Reynolds stress profiles shown in Fig. 4: The model error in the uncontrolled profile (T_4) is the ratio of the weighted area under the black lines (model area in the numerator) in Figs. 4(a) and 4(b), respectively, while the error in turbulent DR (T_3) is the ratio of the weighted area between the black and gray lines (model area in the denominator). The Reynolds stress profiles can therefore be used to estimate the magnitude of both terms: As can be seen from the definition in Eq. (11) and a comparison of the y-axis scale in Figs. 4(a) and 4(b), the magnitude of the model error in the uncontrolled profile is $T_4 \gg 1$. Since $T_3(y_d^+, \angle\hat{A}_d)T_4 = O(1)$, it further follows that the magnitude of the model error in turbulent DR satisfies $T_3(y_d, \angle\hat{A}_d) \ll 1$. Both terms are dominated by the model contribution, which in T_3 appears in the denominator and in T_4 in the numerator. This suggests that the broadband forcing could be rescaled by a constant factor, which would cancel out in the DR measure (12) and bring both terms closer to order one.

The lesser agreement between the model prediction and DNS for more negative shifts further indicates that T_3 increases as $\angle\hat{A}_d$ decreases. This allows us to draw another conclusion regarding the interplay between the control effect in spectral space and the forcing model: The good agreement between the resolvent model, which uses the simplistic broadband forcing, and the DNS for $\angle\hat{A}_d > 0$ suggests that a positive phase amplifies all modes across spectral space. In this scenario, the error arising from the broadband forcing assumption cancels in the ratio $T_3(y_{d,\max}, \angle\hat{A}_{d,\max})/T_3(y_d, \angle\hat{A}_d)$ and the contour levels collapse as observed. On the other hand, the disagreement for $\angle\hat{A}_d < 0$ suggests that the control effect for negative phases is mixed in spectral space, so the model error from the broadband forcing assumption does not cancel. Instead, the broadband forcing puts too much weight on modes which are further suppressed by a negative phase shift, which leads to the observed discrepancy between the model and DNS. This interpretation of Fig. 3 is further confirmed by earlier findings of Luhar *et al.* [13], who show that from a resolvent model perspective, the effect of varying-phase opposition control in spectral space is indeed mixed. Therefore, the more mixed the effect of control in spectral space, the more careful one has to be with the selection of forcing model. However, in this regard the resolvent model with broadband forcing (4) can always be used as a first-order design to estimate the relation between $\mathbf{k}$ and DR and a more refined forcing model can be added in a second step if needed.

It is worth mentioning briefly that Fig. 4 shows another interesting feature of the flow: The controlled Reynolds stress profiles of both the DNS and the resolvent model (gray lines) have a local maximum close to the wall, which is not observed in the uncontrolled case (black lines). The potential link between this feature and drag reduction is beyond the scope of the present work.

Before moving on to analyzing the role of the mean velocity profile, we would like to link and compare the DNS data with results reported in the literature. We first note that the controller with $\angle\hat{A}_d = 0$ is related to the original opposition control scheme of Choi *et al.* [14]: The two schemes are identical except for the mixed-argument term in Eq. (8), which is controlled in the original scheme, but left uncontrolled under the formulation here. The qualitative behaviors of the present and the original schemes are indeed very similar, as can be seen by comparing Fig. 3(b) along $\angle\hat{A}_d = 0$ to results reported in [14,16]: The DR initially increases as the sensor moves away from the wall and a maximum DR is reached at around $y_d^+ = 15$. The DR decreases as y_d is increased further and the control scheme increases drag for sensors located above $y_d^+ = 23$. However, the achievable DR is quite different: For example, the present controller achieves 17% DR for ($y_d^+ = 15$ and $\angle\hat{A}_d = 0$), while the original controller reduced drag by 25% with sensors located at the same location. This indicates that the mixed-argument term in Eq. (8) plays an important role in the drag characteristics of the flow. It is also interesting to compare the effect of the phase shift to related studies in the literature: Kim and Choi [18] found that the maximum drag reduction of opposition control can be increased by adding an integral term to the control law. Integration in the time domain corresponds to a frequency-dependent phase shift in the Fourier domain and our finding that a nonzero $\angle\hat{A}_d$ can increase the maximum drag reduction therefore agrees with their result. Lee [17] further showed that using upstream sensor information increases the maximum DR of opposition control, while using downstream sensor information decreases it. As explained in Sec. II D, a nonzero $\angle\hat{A}_d$ can be interpreted as a streamwise shift of the actuation and our results in Fig. 3(b) indeed confirm that using upstream sensor information can increase the maximum DR, while using downstream sensor information reduces it.

B. Role of the mean velocity profile

Figure 4 further provides an interesting insight into the role of the mean velocity profile in the controlled flow: The resolvent model prediction of the controlled Reynolds stress profile is shown as a solid gray line in Fig. 4(b). It is apparent from the figure that the effect of control on the modeled Reynolds stress profile is localized around the sensor position ($y_d^+ \approx 10$), where an attenuation as well as a slight outward shift of the peak can be observed. The profile remains unchanged above $y \approx -0.8$, as can be seen by comparing the uncontrolled (solid black line) and the controlled (solid gray line) Reynolds stresses. From the perspective of the resolvent model, the Reynolds stress in the outer flow is produced by fast moving modes with no velocity signature close to the wall [13], so these modes cannot be detected by the sensor and therefore remain uncontrolled. Furthermore, recall from Sec. III A that we used the uncontrolled mean velocity profile to construct the resolvent operator, so the outer flow experiences the same τ_w as in the uncontrolled case. From the resolvent perspective there is therefore really no difference in the outer flow between the uncontrolled and the controlled case and it is no surprise that the two profiles coincide.

The DNS [Fig. 4(a)], on the other hand, draws a different picture: A comparison of the uncontrolled (solid black line) and the controlled (solid gray line) profile shows that the Reynolds stress decreases throughout the channel, similar to the results reported by Choi *et al.* [14]. It can be shown from the mean momentum equation that the tilting of the profile in the outer flow is due to a change in u_τ under control. This line of thought cannot be applied to the resolvent model (recall that the model does not satisfy the mean momentum equation), but other ideas, such as Townsend's outer-layer similarity hypothesis [35], also suggest that changes in the outer flow are mainly due to changes in u_τ, without relying on the mean momentum equation. One may therefore speculate that the change in the outer flow can be captured in the resolvent model if a controlled mean with different u_τ is used in the resolvent operator. To test this hypothesis we constructed the resolvent

operator with the controlled DNS mean velocity profile and repeated the model prediction for the example controlled flow ($y_d^+ = 10$ and $\angle\hat{A}_d = -\pi/4$).

The resulting Reynolds stress profile is shown as a dotted orange line in Fig. 4(b). We also plot the Reynolds stress profile with controlled mean but no-slip boundary conditions in Fig. 4(b) to illustrate which changes are due to the change in mean and which ones are due to control at the boundary. It is apparent from the figure that the controlled mean alters the shape of the mean Reynolds stress profile throughout the channel: The near-wall peak is further increased and the Reynolds stresses decrease above $y = -0.8$. The effect of control is again limited to the sensor location. When comparing the uncontrolled profile with uncontrolled mean (black line) to the controlled profile with controlled mean (orange dotted line) it is apparent that the profile is different throughout the channel. This supports the hypothesis that the change in the outer flow is indeed mainly due to the change in u_τ. Also, the predicted DR increases from 5% (uncontrolled mean) to 10% (controlled mean), which is closer to the DNS value of 21%. This suggests that the modeling errors $T_3(y_d^+, \angle\hat{A}_d)T_4$ also decrease when the controlled mean is used.

C. Extension of the model for controller design at high Reynolds numbers

The results thus far have shown how and validated that the resolvent model can be used to design control schemes for internal flows at $\mathrm{Re}_\tau = 180$. The results show that at these low Reynolds numbers the (subsampled) resolvent model is almost two orders of magnitude cheaper to evaluate than DNS, while still capturing the trend observed in the full nonlinear system and therefore making it a valuable design tool in this range of Re_τ. However, DNS is still feasible and relatively cheap at these low Reynolds numbers, so the value of the resolvent model may not be immediately apparent. As mentioned in the Introduction, the ultimate goal is to develop tools that allow controller design for internal flows at technologically relevant Reynolds numbers. Direct numerical simulation is currently limited to relatively low Re_τ, while the resolvent model is not and this is really where the model unlocks its full potential.

Two aspects of the model are crucial for its utility in high-Reynolds-number flows. First is the smoothness of the Reynolds stress profile in at least parts of the wave-number space, which allows us to subsample the model as described in Sec. II C. As was shown for the $\mathrm{Re}_\tau = 180$ case, the contributions of high wave numbers decay quickly, which makes the incorporation of additional high wave numbers cheap as Re_τ increases. The results presented here and in Ref. [8] show that this approach is well justified and allow us to easily handle flows at $\mathrm{Re}_\tau = O(10^4)$ with the model, at least. In a naive approach, one could use the subsampling and proceed at high Reynolds number as outlined in Sec. II B: Use the eddy viscosity to obtain an approximation of the mean velocity profile, construct the resolvent operator, and compute the resolvent modes. Enough resolution is still required in the wall-normal direction to resolve all features of the resolvent modes and this is particularly challenging in the near-wall region where structures scale with viscous units. While the resolution requirements may still be practical at moderate Reynolds number, they become prohibitive at large Re_τ and a different approach is required.

This is where the second aspect of the resolvent model comes in. Moarref *et al.* [8] derived scaling laws for different classes of resolvent modes (categorized based on their wave speed) from the properties of the resolvent operator alone. This allows one to compute resolvent modes at a low Reynolds number, where resolution requirements in y are mild, and use the scaling laws to obtain the singular values and vectors at arbitrary high Reynolds numbers. Here we explore whether the scaling laws also apply to controlled flows by making predictions at two higher Reynolds numbers: $\mathrm{Re}_\tau = 6000$, which is approximately the upper end of available experimental [36] and DNS [28,37] data, and $\mathrm{Re}_\tau = 30\,000$, which is well above current DNS and experimental capabilities and at the lower end of the technologically relevant Reynolds numbers [38]. To illustrate our point, we select the so-called inner class of resolvent modes, which scales in viscous units [8] and is therefore the most challenging to calculate with the naive approach described above. It has been verified that the scaling laws apply to the other classes of modes as well.

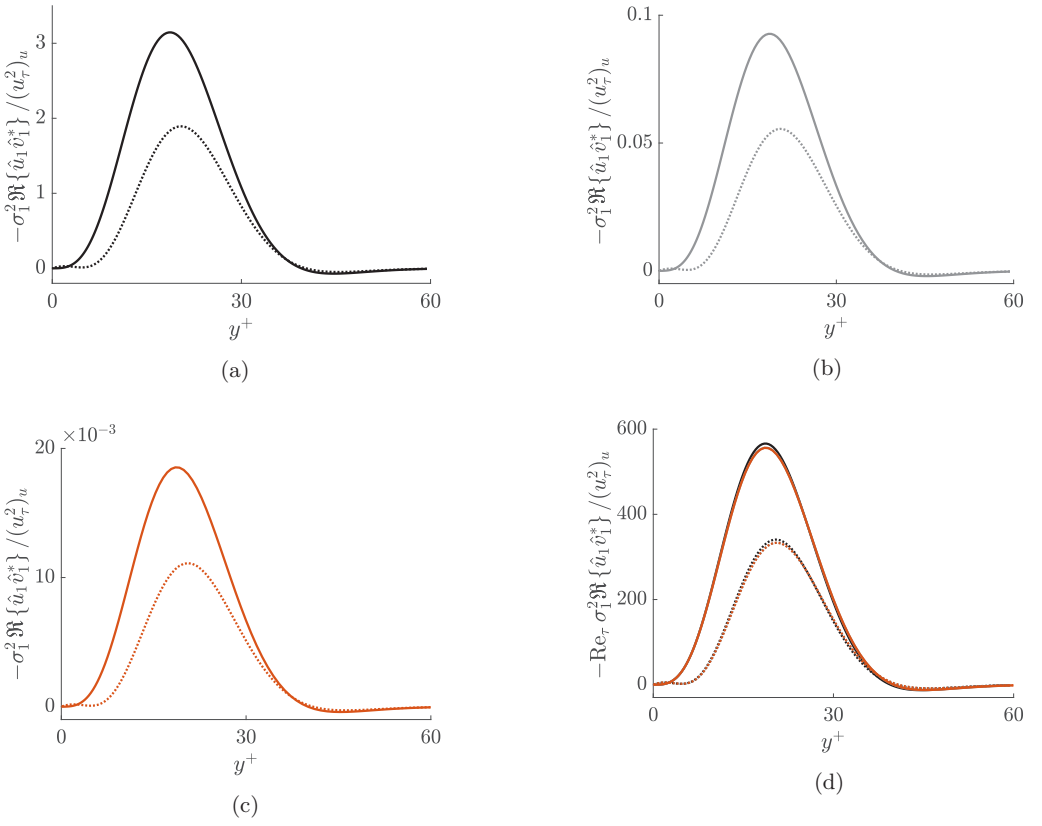

FIG. 5. Mean Reynolds stress contribution of an example resolvent mode characterized by $\lambda_x^+ = 1000$, $\lambda_z^+ = 100$, and $c^+ = 10$ at (a) $\mathrm{Re}_\tau = 180$ (——), (b) $\mathrm{Re}_\tau = 6000$ (——), and (c) $\mathrm{Re}_\tau = 30\,000$ (——). In all figures, the solid line shows the profile of the uncontrolled flow, while the dotted line displays the profile of an example controlled flow ($y_d^+ = 10$ and $\angle\hat{A}_d = -\pi/4$). (d) Same profiles rescaled according to the Reynolds number scaling law introduced by Moarref *et al.* [8].

Figures 5(a)–5(c) show the mean Reynolds stress contribution of a single resolvent mode characterized by $\lambda_x^+ = 1000$, $\lambda_z^+ = 100$, and $c^+ = 10$, where the solid and dotted lines represent the uncontrolled flow and an example controlled flow ($y_d^+ = 10$ and $\angle\hat{A}_d = -\pi/4$), respectively. Note that this mode belongs to the inner class according to the classification by Moarref *et al.* [8]. These resolvent modes are computed using the naive approach, i.e., we computed the resolvent modes directly at the indicated Reynolds numbers. To obtain DNS resolution, one would require $N_y = 172$, 1700, and 8500 grid points in the wall-normal direction (with an appropriate grid stretching factor in the high-Re cases), respectively. However, the singular values are already converged for $N_y = 90$, 130, and 300, respectively. We therefore used somewhat coarser grids with $N_y = 172$, 800, and 1230 (without grid stretching to ensure sufficient resolution in the near-wall region) to produce the results shown in Figs. 5(a)–5(c). It can first be observed that the energy content of the near-wall structure decreases as the Reynolds number increases. Moreover, the plots suggest that the shape of the structure remains unchanged with increasing Reynolds number. In fact, the mean Reynolds stress contributions follow the scaling law proposed by Moarref *et al.* [8]: As shown in Fig. 5(d), the profiles across all Reynolds numbers collapse when scaled appropriately. The scaling therefore holds not only in the uncontrolled flow, which was already shown in [8], but also in the controlled flow. This is a key property of the model that allows the naive approach to be superseded by far:

There is no need to compute the resolvent modes at high Re_τ. All one has to do is compute the resolvent modes at low Reynolds number, which is cheap, and then use the known scaling laws to obtain their contribution at an arbitrary high Re_τ.

We close this section with two comments. First, it should be noted that the scaling laws assume the presence of a logarithmic region in the mean velocity profile [8]. The empirical results of Fig. 5 show good agreement between all the profiles, but strictly speaking at least $\mathrm{Re}_\tau = 180$ is too low to argue for the existence of a logarithmic region. In fact, there is a slight deviation between the $\mathrm{Re}_\tau = 180$ profile and the two other ones which may be a Reynolds-number effect, even if small. One may therefore consider a slightly higher Reynolds number when generating the profiles for scaling. Second, there is a small subset of wave-number combinations that do not belong to any similarity class (see Moarref *et al.* [8] for details). Depending on their significance in the resolvent model, these modes may have to be computed explicitly at high Reynolds numbers. Note, however, that when combined with the subsampling strategy, this is only required for very few modes.

V. CONCLUSION

This study analyzed the drag reduction of varying-phase opposition control by means of a low-order resolvent model and a DNS. Great care was taken to ensure that both frameworks represent the same flow, resolve the same range of scales, and implement an equivalent flow control law.

The first part of this study concerned the review of a resolvent model, which was derived from the incompressible Navier-Stokes equations using the simplest assumptions possible: formulation of the resolvent operator based on an uncontrolled mean velocity profile, rank-1 approximation, and broadband forcing assumption. The resolution of the model baseline was chosen to match the DNS, so model errors due to resolution discrepancies could be ruled out. A mode-by-mode analysis of the Reynolds stress profile suggested that the wave-number space can be subsampled when evaluating the resolvent model. The good agreement between the model baseline and the subsampled model, which only resolves 2% of the baseline wave numbers, confirmed the validity of this hypothesis (see Fig. 1) and suggests that for this flow the resolvent model is lower dimensional than the DNS. However, this could only be confirmed once the model baseline provided an adequate benchmark for comparison with DNS. While similar subsampling strategies were already used in the past (see, for example, [8,13]), the present study systematically confirms the accuracy of the subsampled model and thus provides a formal justification for this approach. Why one gets away with sampling such a small subset of wave numbers is yet to be fully understood. Further progress on this question may help guide the development of novel simulation techniques which in the spirit of the subsampled resolvent model do not resolve all scales, but only the dynamically most relevant ones.

The subsequent formulation of the varying-phase opposition control law highlighted the importance of understanding the assumptions and resulting limitations of the resolvent model. With the current assumptions the model framework only captures a subset of the physics of the full nonlinear system and a naive implementation of the controller would have led to different control effects in the resolvent model and the DNS. A separate control law for the streamwise constant modes was sufficient to reconcile both frameworks in the present case, but studies concerned with different flows or control objectives may need to relax more fundamental assumptions if the relevant physics is not represented in the model. For example, Rosenberg *et al.* [39] recently outlined conditions (more commonly encountered in bluff body flows) under which the rank-1 approximation employed here may be insufficient to capture the essential flow physics. The FIK identity and mean momentum equation were used to derive an analytical expression for the conventional drag reduction measure as a product of four terms with clear physical interpretation (ratio of turbulent drag to total drag, modeled turbulent drag reduction, model error in turbulent drag reduction, and model error in uncontrolled profile). Using this expression, it was shown that the model is able to approximate not only the turbulent drag reduction, but also the change in mean wall shear stress. The expression further allows one to quantify the two model error sources (error in the uncontrolled profile and error in the turbulent DR) if higher fidelity data are available for comparison.

The centerpiece of this study was based on varying-phase opposition control: The normalized DR predicted by the resolvent model for various sensor locations y_d and phase shifts $\angle\hat{A}_d$ was compared with DNS data. Even though the model was formulated with very strong assumptions, the normalized DR maps of the resolvent model and the DNS agreed remarkably well (see Fig. 3). The DNS data confirmed the resolvent model prediction that the attainable drag reduction strongly depends on the relative phase between sensor measurement and actuator response. This raises interesting questions about the role of the phase in the flow. The large parameter space explored in this study by means of the resolvent model and DNS provides a rich database to evaluate the capabilities of the resolvent model and thus allows us to draw strong conclusions. The degree of agreement reveals that resolvent analysis, which at its heart is a linear technique, can approximate the response of the full nonlinear system to control and allays doubts that may have persisted thus far. As a consequence, one of the questions posed at the beginning of this study can be answered in the affirmative: The results suggest that the resolvent model is indeed a suitable low-order flow model to design active flow control schemes for drag reduction in internal flows. This gives a formal foundation to recent studies which already use the resolvent model for controller design, such as [23], and provides a tool to systematically design future controllers. Since there is nothing particular about the choice of varying-phase opposition control, we expect that the resolvent model is able to approximate the DR trend of any control scheme with linear control law as long as the controlled mean velocity profile is not too drastically different from the uncontrolled one. The study also outlined limitations of the model: The simplistic broadband forcing may be inappropriate if the effect of control is mixed in spectral space. To what degree the control effect varies in wave-number space can be estimated from the resolvent model presented here and more sophisticated forcing models can be incorporated in a second step, if needed. Furthermore, if the mean velocity profile is modified substantially, for example, due to large-scale changes of the flow structure in any part of the flow, then it is not likely that the resolvent operator derived from the uncontrolled mean can correctly identify DR trends. There is currently no rigorous measure for when resolvent analysis based on the uncontrolled mean is not applicable, but the present study suggests that the restrictions on the change in mean velocity profile are not as stringent as one may think: For example, the Reynolds number varies by more than a factor of 2 over the parameter space shown in Fig. 3 and yet the resolvent model is able to capture the DR trend of the full nonlinear system. The effect of a relatively small change in mean velocity profile on the resolvent prediction was further shown in Fig 4(b): The model suggests that while the change in boundary condition leads to a localized decrease in Reynolds stress around the sensor location, the change in mean velocity profile is responsible for the attenuation further away from the wall.

At low Reynolds number, the resolvent model was shown to be almost two orders of magnitude cheaper to evaluate than a DNS. However, the model unlocks its full potential at high Reynolds numbers, which are currently not feasible with DNS. The last part of this study showed that the known Reynolds-number scaling of resolvent modes also holds in the controlled case. This allows one to do resolvent analysis at low Re_τ, which is cheap, and use the scaling laws to obtain the singular values and vectors at arbitrary high Reynolds numbers, essentially for free. Luhar *et al.* [13] further showed that the resolvent model presented here is able to capture Reynolds-number trends previously observed in DNS of controlled flows. Their result, combined with the scaling laws, suggests that the second point raised in the Introduction can also be answered in the affirmative: It can be expected that the resolvent model can be used to design controllers at technologically relevant Reynolds numbers, which are currently not feasible with DNS.

Future work may explore whether a hierarchy of models can be used to further reduce the computational cost of controller design: For a first-order design, one may not have to evaluate the resolvent model at all the subsampled DNS wave numbers, but only at an even smaller subset like, for example, the wave numbers representing the near-wall cycle. The first-order controller design can subsequently be refined using the resolvent model presented here and finally be validated in a DNS or experiment. Future studies may also explore control design at high Reynolds numbers using the resolvent model in combination with the presented scaling laws. In this context, it would

be interesting to explore if the broadband forcing assumption is still a good model or if the weights should be scaled with Reynolds number as well, similar to previous work by Moarref *et al.* [8].

ACKNOWLEDGMENTS

The authors gratefully acknowledge the U.S. Air Force Office of Scientific Research (Grant No. FA 9550-16-1-0361) for financial support of this work and a graduate fellowship (S.S.T.) from the Resnick Sustainability Institute at Caltech. We would also like to thank J. Jiménez for making his channel DNS code available, P. Koumoutsakos for providing the computational resources for this study, and the reviewers for their feedback, which has greatly improved the quality of this paper.

[1] I. Marusic, R. Mathis, and N. Hutchins, Predictive model for wall-bounded turbulent flow, Science **329**, 193 (2010).
[2] M. Gad-el-Hak, *Flow Control: Passive, Active, and Reactive Flow Management* (Cambridge University Press, Cambridge, 2000).
[3] B. J. McKeon and A. S. Sharma, A critical-layer framework for turbulent pipe flow, J. Fluid Mech. **658**, 336 (2010).
[4] L. N. Trefethen, A. E. Trefethen, S. C. Reddy, and T. A. Driscoll, Hydrodynamic stability without eigenvalues, Science **261**, 578 (1993).
[5] K. M. Butler and B. F. Farrell, Optimal perturbations and streak spacing in wall-bounded turbulent shear flow, Phys. Fluids A **5**, 774 (1993).
[6] B. J. McKeon, The engine behind (wall) turbulence: Perspectives on scale interactions, J. Fluid Mech. **817**, P1 (2017).
[7] P. Holmes, J. L. Lumley, G. Berkooz, and C. W. Rowley, *Turbulence, Coherent Structures, Dynamical Systems and Symmetry*, 2nd ed. (Cambridge University Press, Cambridge, 2012).
[8] R. Moarref, A. S. Sharma, J. A. Tropp, and B. J. McKeon, Model-based scaling of the streamwise energy density in high-Reynolds-number turbulent channels, J. Fluid Mech. **734**, 275 (2013).
[9] M. Luhar, A. S. Sharma, and B. J. McKeon, On the structure and origin of pressure fluctuations in wall turbulence: Predictions based on the resolvent analysis, J. Fluid Mech. **751**, 38 (2014).
[10] R. Moarref, M. R. Jovanović, J. A. Tropp, A. S. Sharma, and B. J. McKeon, A low-order decomposition of turbulent channel flow via resolvent analysis and convex optimization, Phys. Fluids **26**, 051701 (2014).
[11] A. Zare, M. R. Jovanović, and T. T. Georgiou, Colour of turbulence, J. Fluid Mech. **812**, 636 (2017).
[12] A. Towne, O. T. Schmidt, and T. Colonius, Spectral proper orthogonal decomposition and its relationship to dynamic mode decomposition and resolvent analysis, J. Fluid Mech. **847**, 821 (2018).
[13] M. Luhar, A. S. Sharma, and B. J. McKeon, Opposition control within the resolvent analysis framework, J. Fluid Mech. **749**, 597 (2014).
[14] H. Choi, P. Moin, and J. Kim, Active turbulence control for drag reduction in wall-bounded flows, J. Fluid Mech. **262**, 75 (1994).
[15] K. Fukagata and N. Kasagi, in *Engineering Turbulence Modelling and Experiments 5*, edited by W. Rodi and N. Fueyo (Elsevier Science, Oxford, 2002), pp. 607–616.
[16] Y. M. Chung and T. Talha, Effectiveness of active flow control for turbulent skin friction drag reduction, Phys. Fluids **23**, 025102 (2011).
[17] J. Lee, Opposition control of turbulent wall-bounded flow using upstream sensor, J. Mech. Sci. Technol. **29**, 4729 (2015).
[18] E. Kim and H. Choi, Linear proportional–integral control for skin-friction reduction in a turbulent channel flow, J. Fluid Mech. **814**, 430 (2017).
[19] B.-Q. Deng, W.-X. Huang, and C.-X. Xu, Origin of effectiveness degradation in active drag reduction control of turbulent channel flow at $\mathrm{Re}_\tau = 1000$, J. Turbul. **17**, 758 (2016).
[20] J. Lim and J. Kim, A singular value analysis of boundary layer control, Phys. Fluids **16**, 1980 (2004).

[21] C. A. Duque-Daza, M. F. Baig, D. A. Lockerby, S. I. Chernyshenko, and C. Davies, Modelling turbulent skin-friction control using linearized Navier-Stokes equations, J. Fluid Mech. **702**, 403 (2012).
[22] S. Nakashima, K. Fukagata, and M. Luhar, Assessment of suboptimal control for turbulent skin friction reduction via resolvent analysis, J. Fluid Mech. **828**, 496 (2017).
[23] A. Kawagoe, S. Nakashima, M. Luhar, and K. Fukagata, Proposal of control laws for turbulent skin friction reduction based on resolvent analysis, J. Fluid Mech. **866**, 810 (2019).
[24] C.-A. Yeh and K. Taira, Resolvent-analysis-based design of airfoil separation control, J. Fluid Mech. **867**, 572 (2019).
[25] C. Leclercq, F. Demourant, C. Poussot-Vassal, and D. Sipp, Linear iterative method for closed-loop control of quasiperiodic flows, J. Fluid Mech. **868**, 26 (2019).
[26] O. Flores and J. Jiménez, Effect of wall-boundary disturbances on turbulent channel flows, J. Fluid Mech. **566**, 357 (2006).
[27] J. Kim, P. Moin, and R. Moser, Turbulence statistics in fully developed channel flow at low Reynolds number, J. Fluid Mech. **177**, 133 (1987).
[28] M. Lee and R. D. Moser, Direct numerical simulation of turbulent channel flow up to $Re_\tau \approx 5200$, J. Fluid Mech. **774**, 395 (2015).
[29] W. C. Reynolds and W. G. Tiederman, Stability of turbulent channel flow, with application to Malkus's theory, J. Fluid Mech. **27**, 253 (1967).
[30] J. C. del Álamo and J. Jiménez, Linear energy amplification in turbulent channels, J. Fluid Mech. **559**, 205 (2006).
[31] J.-L. Bourguignon, J. A. Tropp, A. S. Sharma, and B. J. McKeon, Compact representation of wall-bounded turbulence using compressive sampling, Phys. Fluids **26**, 015109 (2014).
[32] K. M. Butler and B. F. Farrell, Three-dimensional optimal perturbations in viscous shear flow, Phys. Fluids A **4**, 1637 (1992).
[33] J. Kim and T. R. Bewley, A linear systems approach to flow control, Annu. Rev. Fluid Mech. **39**, 383 (2007).
[34] K. Fukagata, K. Iwamoto, and N. Kasagi, Contribution of Reynolds stress distribution to the skin friction in wall-bounded flows, Phys. Fluids **14**, L73 (2002).
[35] A. A. Townsend, *The Structure of Turbulent Shear Flow*, 1st ed. (Cambridge University Press, Cambridge, 1956).
[36] M. P. Schultz and K. A. Flack, Reynolds-number scaling of turbulent channel flow, Phys. Fluids **25**, 025104 (2013).
[37] Y. Yamamoto and Y. Tsuji, Numerical evidence of logarithmic regions in channel flow at $\mathrm{Re}_\tau = 8000$, Phys. Rev. Fluids **3**, 012602 (2018).
[38] A. J. Smits and I. Marusic, Wall-bounded turbulence, Phys. Today **66**(9), 25 (2013).
[39] K. Rosenberg, S. Symon, and B. J. McKeon, Role of parasitic modes in nonlinear closure via the resolvent feedback loop, Phys. Rev. Fluids **4**, 052601 (2019).